Published in
Int. J. of Solids and Structures
161 (2019), 219–227

Finite difference model of wave motion for Structural Health Monitoring of Single Lap Joints

Stefano Carrino, Francesco Nicassio, Gennaro Scarselli

Department of Innovation Engineering, University of Salento, Lecce, Italy

Raffaele Vitolo

Department of Mathematics and Physics "E. De Giorgi", University of Salento, Lecce, Italy

Abstract

This study is focused on the development of a finite difference model to simulate Lamb wave propagation through Single Lap Joints (SLJs). The main advantage of this model is the mathematical ability to easily reproduce the presence of a damage (debonding) as a discontinuity in velocity values. This makes our model suitable for continuous and embedded Structural Health Monitoring (SHM) of a complex structure. Numerical simulations and experimental campaigns are presented in order to validate the proposed model.

Keywords: Finite difference model, Lamb waves, structural health monitoring, single lap joints.

1. Introduction

Adhesive joints are used in aerospace, automotive and marine industries for their good mechanical properties and light weight. For several structural applications, they represent the only feasible method of joining components with advantages in terms of cost, optimal stress distribution and ease of

Email addresses: stefano.carrino@unisalento.it, francesco.nicassio@unisalento.it, gennari.scarselli@unisalento.it (Stefano Carrino, Francesco Nicassio, Gennaro Scarselli), raffaele.vitolo@unisalento.it (Raffaele Vitolo)

manufacturing. Bonded joints distribute forces over a large area avoiding stress peaks that could arise by using fasteners like bolts, rivets or screws.

Despite these positive aspects, bonded joints are subject to fatigue degradation of the adhesive layer, disbonds and voids due to non-accurate manufacturing processes that reduce the load carrying capability, leading to failure as studied in [11].

For the above reasons, the development of SHM systems is necessary in order to ensure reliability and safety of adhesively bonded joints in complex structures. SHM also contributes to a better knowledge of the mechanical properties of the structures [31]. Over the past decades, several studies have been carried out on investigating the dynamic response of the adhesive joints and the development of efficient Non-Destructive Techniques (NDT) in order to detect, evaluate and localise defects or damages eventually present in bonded areas.

Conventional NDT are of limited use because they require to put out of service the structure for a non-negligible time period in order to execute post-damage inspections. In addition to the Visual Testing (VT), which is by far the most common non-destructive examination, Ultrasonic A- and C-scan, X-ray and thermography can be employed to inspect structural components. In ultrasonic scanning, a transducer generates pulses of shear or compression waves at frequency of 1 to 20 MHz that, during the propagation through the adhesion zone, is modified by the path taken and a part of energy is reflected by discontinuities. A- and C-scan consist in the evaluation of the magnitude of the reflected echoes thus obtaining a map of defects by scanning the surface of a structure. In [27] a non-destructive testing of the lower and upper wing skins was performed by use of an A- and C-scan transducer obtaining information regarding the condition of composites and the integrity of the composite-to-titanium bonded joint. A large defect was found in a lower wing skin outlining the boundary and the location of defect through the thickness.

X-ray techniques, in contrast to ultrasound and thermography, can provide a 3D image of a damage. In [21] a methodology to evaluate the through-thickness distribution of damage in a $[(0^o/90^o)_2]_S$ Carbon Fibre Reinforced Plastic (CFRP) panels subjected to low velocity impact is developed: delaminations were mapped by a 3D ply-by-ply damage visualisation.

An Infrared (IR) NDT of interlaminar disbonds on fibre metal laminate hybrid composites was proposed in [26]: a point-wise laser heat source (Flying Laser Spot Thermography) was moved along a raster scanning tra-

jectory over the structure surface; an IR camera was employed to acquire the temperature field induced by the moving heat source; disbonds and defects were then detected by analysing the perturbations of the temperature distribution.

Yashiro et al. in [36] evaluated fatigue-induced disbond in CFRP double-lap joints using embedded Fibre Bragg Grating (FBG) sensors. The study is based on a change in the spectrum shapes of FBG sensors embedded near the bond-line. These sensors experienced a step-like strain distribution due to the intact load-carrying section and the disbonded stress-free section. The disbond area was determined from the evaluation of the reflection spectrum of FBG sensors embedded in different lines of a joint.

In [24] adhesively bonded CFRP samples were investigated by using ElectroMechanical Impedance (EMI) technique. This is based on direct and converse effects of piezoelectric sensor (PZT) attached on the inspected structure. The electrical response picked up on the sensor is related to mechanical characteristics of the structure and then to the modification of adhesive bonds. Various techniques are based on nonlinear acoustics methods: the Contact Acoustic Nonlinearity (CAN) ([34], [6]), vibro-acoustics wave modulation, nonlinear elastic wave spectroscopy and the Local Defect Resonance (LDR) ([33], [8]). LDR is based on the local rigidity decrease of a certain mass associated with the defect area which causes the arising of a specific frequency related to the characteristic of the defect. In [8] the use of nonlinear waves for detection of disbonds in adhesive joints was investigated. Subharmonics, nonlinear intermodulation of the driving frequency and defect resonance frequencies were correlated to the interaction between the used elastic waves and disbonded regions.

One of the most promising techniques that enables inspections at long distances is based on the application of Ultrasonic Guided Waves (UGWs) [9, 19] such as acousto-ultrasonic induced Lamb waves. This technique consists in exciting Lamb waves by a piezoelectric transducer attached to the structure's surface which can be detected by a network of multiple sensors. The presence of defects or damages in the investigated domain alters the signal propagation, resulting in a received signal which is different from the one that was initially generated.

Non-linear ultrasonic waves are used also in [30] for assessment of debonding in SLJ: the presence of microbubbles in the bond due to the manufacturing process was investigated by interpretating the experimental behaviours and tomographic tests. In [32] the phase and the amplitude of the structural

SLJ response excited by an harmonic excitation was evaluated in order to characterise defects and damages within the adhesive region according to the dynamic response. In [25] an experimental investigation of the use of Lamb waves for the monitoring of stiffened metallic structures was carried out: the size and shape of defect was evaluated and visualised by a windowed root-mean-squared technique for quantifying of reflected, attenuated and transmitted energy. A baseline-free technique is proposed in [28] which is based on the detection of modes generated by disbonds. It was demonstrated that the disbond caused reflection, refraction and mode conversion of the incident S0 wave. Several sensors distributed parallel to the edge of bonded area allow the identification of disbonds by the appearance of wave modes.

Jankauskas and Mazeika in [13] carried out a numerical and experimental study of zero-mode Lamb waves propagation through a lap joint welded plates used in storage tank floors. It was demonstrated that the transmission losses of the S0 mode vary depending on the ratio between lap joint width and wavelength providing information for the defect or damage geometry definition. A mode similar to S0 Lamb wave propagation was used in [7] that can be used for inspection of large welded plate so to detect defects such as cracking or corrosion along the length of weld. Huthwaite in [12] used guided wave tomography to produce thickness maps of corrosion damage and defects by sending guided waves through the studied region.

In [3] fundamental Lamb wave modes was characterised in terms of propagation parameters through Finite Element Method (FEM) in commercial software in order to study the wave behaviour on a plate between two solid bodies with imperfect contact conditions. Ren and Lissenden in [29] carried out a fully coupled multi-physics finite element analysis, which includes the driving circuit and the piezoelectric elements, in order to study the excitation of circular crested waves due to PZT discs for different sensor geometry and adhesive thickness. In [15] a semi-analytical finite element (SAFE) method wad used to model the distributed electrical excitation and scattering of the waves at discontinuities by using piezoelectric elements. The Lamb waves were modelled by Spectral Element Method (SEM) as in [23] and [20]. Liu et al. in [22] presented a two-layer spectral finite element model to simulate PZT-induced Lamb wave propagation in beam-like and plate-like structures where the dynamic equation was derived from Hamilton's principle.

A Finite Difference Method (FDM) was used in ([35], [2], [14]) to simu-

late multiple modes of Lamb waves in aluminium SLJ generated by using an excitation toneburst representing the PZTs action. In [35] an explicit Finite Difference (FD) scheme was applied to solve propagating Lamb waves. Balasubramanyam in [2] describes a FDM to simulate S0 and A0 in plane metal sheets obtaining the time-domain histories of displacement field. In [14] the excitation and propagation of Lamb waves by inter-digital transducer was modelled analytically and then compared to experimental measure obtained by exciting Lamb waves in an aluminium plate.

For the sake of completeness, the papers [5, 16, 17, 18] shall be mentioned. Here, nonlinear wave equations of KdV, Boussinesq or other types were considered as mathematical models. It was proved, both mathematically and experimentally, that solitons traveling in a delaminated material are subject to fission, hencey they are suitable to detecting defects. This technique, however, has a higher level of experimental complexity involving the use of laser and optical equipment, also if it might be more suitable than the technique presented in this paper in the case of long elastic waveguides.

Although the techniques mentioned are suitable to assess the health of bonded areas, only UGWs allow the *continuous* and *embedded* time monitoring of the structures.

In this work a numerical and experimental investigation of Single Lap Joints (SLJs) structural health by using Lamb waves propagation is presented. The aim was to monitor the state of adhesive region and estimate the size of possible disbonds.

The paper is divided in two part: the mathematical model and its numerical implementation, and the experimental part.

The mathematical model stems from the Cauchy–Navier equation for elastodynamics [10]. The key feature lies in the fact that the space-dependent Lamé coefficients have discontinuity on the boundary with the debonded region. The discretisation of this equation has to be performed by keeping into account that the derivatives of the Lamé coefficients will contribute to the FDM.

Experiments on the propagation of S0 through the adhesive zone were performed by using two PZT sensors attached on the upper and lower plate in pitch&catch configuration. The S0 mode was used to investigate the integrity of adhesive in bonded zone. Frequencies below the cut-off value were used in order to avoid the presence of higher symmetric and antisymmetric modes. The received signals were transformed by Fast Fourier Transform (FFT) in order to correlate frequency spectra to the structural health of

adhesive. Several wave packets with different driving frequencies were used to investigate the bonded area. Experiments revealed, in agreement with numerical simulations, that for each disbond length there is a given driving frequency at which the wave packet is attenuated and presents a deformed shape of frequency spectrum.

In this way, for SLJ structure, a novel reduced-order FD model is obtained and it appears leaner, cleaner and more simplified than FE model. The fact that numerical simulations were carried out by a relatively simple Matlab code with a short execution time represents one point of strength of the proposed approach, also in view of industrial applications.

2. The model

We make use of Cauchy–Navier's equation for elastodynamics [10]:

$$\rho \mathbf{u}_{tt} = \mu \Delta \mathbf{u} + (\lambda + \mu) \nabla (\operatorname{div} \mathbf{u}) + 2 \widehat{\nabla} \mathbf{u} \nabla \mu + (\operatorname{div} \mathbf{u}) \nabla \lambda + \rho \mathbf{f} \tag{1}$$

where $\mathbf{u}$ is the displacement vector field, λ and μ are the Lamé coefficients (that in our case depend on the spatial point), ρ is the (space-dependent) density and $\mathbf{f}$ is the force per unit mass. We also recall that

$$\widehat{\nabla} \mathbf{u} = \frac{1}{2} (\nabla \mathbf{u} + \nabla \mathbf{u}^T) \tag{2}$$

We use the above equations as a model for a horizontal plate where elastic waves propagate in the x and z direction. The displacement of particles occur both in the direction of propagation and along the thickness of the plate (y-direction). If the domain of equation (1) is a plane perpendicular to the z axis, passing through the application point of $\mathbf{f}$, there is no displacement in the third direction z, hence our problem becomes 2-dimensional.

Let us introduce the notation $\mathbf{u} = (u(x, y), v(x, y))$ for the displacements in the x, y directions, respectively, and the notation $\mathbf{f} = (f_x(x, y), f_y(x, y))$ for the force per unit mass. Then the system (1) becomes

$$\begin{aligned}
\rho u_{tt} =& \mu(u_{xx} + u_{yy}) + (\lambda + \mu)(u_{xx} + v_{xy}) + && \text{(3a)} \\
& (2u_x \mu_x + (u_y + v_x)\mu_y) + (u_x + v_y)\lambda_x + \rho f_x && \text{(3b)} \\
\rho v_{tt} =& \mu(v_{xx} + v_{yy}) + (\lambda + \mu)(u_{xy} + v_{yy}) + && \text{(3c)} \\
& ((u_y + v_x)\mu_x + 2v_y \mu_y) + (u_x + v_y)\lambda_y + \rho f_y && \text{(3d)}
\end{aligned}$$

Provided we neglect terms multiplied by ρ_x or ρ_y (they give a small contribution in our physical situation), we can recast the above equations in the following form:

$$\left(\frac{\lambda+2\mu}{\rho}u_x+\frac{\lambda}{\rho}v_y\right)_x+\left(\frac{\mu}{\rho}(u_y+v_x)\right)_y+f_x=u_{tt} \tag{4a}$$

$$\left(\frac{\mu}{\rho}(u_y+v_x)\right)_x+\left(\frac{\lambda}{\rho}u_x+\frac{\lambda+2\mu}{\rho}v_y\right)_y+f_y=v_{tt} \tag{4b}$$

We add to the above model stress-free boundary conditions on the upper and the lower surfaces of the plate:

$$\frac{\lambda}{\rho}u_x+\frac{\lambda+2\mu}{\rho}v_y=0 \tag{5a}$$

$$\frac{\mu}{\rho}(u_y+v_x)=0 \tag{5b}$$

Usually, the above equations are expressed through the longitudinal wave speed c_L and the shear wave speed c_T:

$$c_L^2=\frac{\lambda+2\mu}{\rho},\qquad c_T^2=\frac{\mu}{\rho}, \tag{6}$$

and we have

$$\big(c_L^2u_x+(c_L^2-2c_T^2)v_y\big)_x+\big(c_T^2(u_y+v_x)\big)_y+f_x=u_{tt} \tag{7a}$$

$$\big(c_T^2(u_y+v_x)\big)_x+\big((c_L^2-2c_T^2)u_x+c_L^2v_y\big)_y+f_y=v_{tt} \tag{7b}$$

with boundary conditions

$$(c_L^2-2c_T^2)u_x+c_L^2v_y=0 \tag{8a}$$

$$c_T^2(u_y+v_x)=0 \tag{8b}$$

3. Finite difference method

We model the domain of the unknown functions u, v as $I_x\times I_y\times I_t$, where

$$I_x=[0,l_x],\quad I_y=[0,l_y],\quad I_t=[0,l_t], \tag{9}$$

with l_x, l_y and l_t positive constants. The space and time grid of the problem is constructed by an equal increment $\Delta x = \Delta y$ in the x and y directions, and a time interval Δt. Following [1], we require that

$$\Delta t \leq \frac{\Delta x}{\sqrt{c_L^2 + c_T^2}} \tag{10}$$

for stability. This amounts at requiring that the signals will not propagate across one grid rectangle in a time that is shorter than one time interval. We assume that the numbers $N_x = l_x/\Delta x$ and $N_y = l_y/\Delta y$ are integer, possibly by redefining the intervals to the nearest values l_x or l_y. We will index points (x_i, y_j) with $1 \leq i \leq N_x + 2$, $1 \leq j \leq N_y + 2$, where

$$x_1 = -\Delta x \qquad x_{N_x+2} = l_x + \Delta x \tag{11}$$

$$y_1 = -\Delta y \qquad y_{N_y+2} = l_y + \Delta y \tag{12}$$

so that the nodes x_1, y_1, x_{N_x+2}, y_{N_y+2} are indeed pseudo-nodes (they lie outside the domain, see Figure 1). Finally, we suppose that $N_t = l_t/\Delta t$ is an integer.

The functions c_L, c_T and ρ are functions of (x, y), and they are non-constant as their values change in the spatial points where the bonding is no longer homogeneous. In this work, we suppose that the non-homogeneity of the bonding holds along the x direction only. In particular, we assume that there is an interval $[x_I, x_F] \subset I_x$ where the bonding is loose. We define the function c_L on the grid according with the above model as follows:

$$c_L(i,j) = \begin{cases} c_L^1 & \text{if} \quad x_i \notin [x_I, x_F], \\ c_L^2 & \text{if} \quad x_i \in [x_I, x_F], \end{cases} \tag{13}$$

where c_L^1 and c_L^2 are two constants. We make a similar definition for c_T and ρ. In the Figure 1 the top picture represents a geometric section of the SLJ sample used for the experiments: it is possible to identify the position of the two sensors, PZT–1 exciting the structure and PZT–2 receiving the signal. In addition, it is possible to identify the two zones of the upper plate forming the joint, 1 and 2, in which the wave travels at different speeds, c_L^1 and c_L^2. The zone 1 is affected only by the aluminum properties and the Lamb waves propagate like in a 1.2 mm thick aluminum panel. The zone 2 is characterised by the influence of the aluminum–adhesive–aluminum layer and c_L^2 depends on the global joint thickness and on the mechanical properties of aluminum and adhesive. Having this in mind, the zone 2 has the

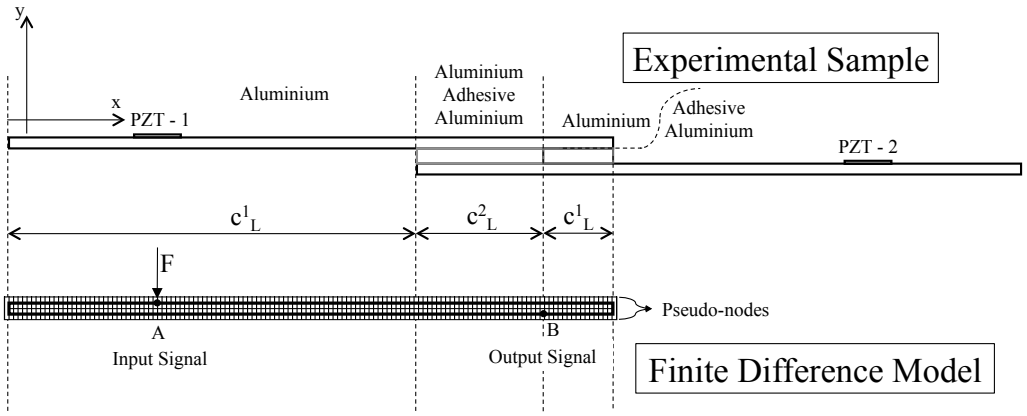

Figure 1: SLJ finite difference model

thickness of the upper plate but mechanical properties averaged over the thickness. The bottom picture represents the grid defined for solving the wave propagation equation and this grid represents geometrically just the volume of the upper plate with properties following what before discussed. The point A represents the excitation point where the F force (due to the PZT–1 action) operates. The point B represents the point where the propagating wave is observed (output signal). The difference between the signal in B and the signal in PZT–2 position is just due to the signal attenuation through the material that is very small: the signal shape remains essentially unaltered.

Then, we define the source of the mechanical impulse by the following function:

$$F\colon I_t \to \mathbb{R}, \quad t \mapsto$$
$$\begin{cases} A\left((1-\cos\left(\frac{2\pi\nu}{N_i}(t-2\Delta t)\right)\right)\sin(2\pi\nu(t-2\Delta t)) & \text{if} \quad t\in[t_I,t_F], \\ 0 \quad \text{otherwise}, \end{cases} \tag{14}$$

where A is a given amplitude, $t_I = 2\Delta t$, N_i is the number of impulses of the probe signal, ν is the frequency of the probe signal and $t_F = N_i/\nu + 2\Delta t$. This is a smoothed tone burst obtained from a pure tone filtered through an Hanning window. The tone burst excitation was chosen in order to use coherent single-frequency wave minimising the dispersive behaviour. The windowing function reduces the excitation of side frequencies associated with the sharp transition at the start and the end of a conventional burst. The choice of N_i and frequency determines the length of the wave packet

that has to be not too long in order to avoid the interference with the reflection due to the boundaries. Thus, bursts with less peaks are chosen for the lower values of frequency used.

We should define the equations for the discrete unknowns $u(i,j,k)$ and $v(i,j,k)$, where i denotes the point x_i, j stands for y_j and k stands for t_k. We proceed as follows: compute x and y derivatives in the equations (7), then replace the derivatives of the given and unknown functions with the following discrete quantities:

$$u_x(i,j,k) = \frac{1}{2\Delta x}(u(i+1,j,k) - u(i-1,j,k)), \tag{15a}$$

$$u_y(i,j,k) = \frac{1}{2\Delta y}(u(i,j+1,k) - u(i,j-1,k)), \tag{15b}$$

and analogously for v, and

$$(c_L)_x(i,j) = \frac{1}{2\Delta x}(c_L(i+1,j) - c_L(i-1,j)), \tag{15c}$$

$$(c_L)_y(i,j) = \frac{1}{2\Delta y}(c_L(i,j+1) - c_L(i,j-1)), \tag{15d}$$

and analogously for c_T, ρ, and

$$u_{xx}(i,j,k) = \frac{1}{\Delta x^2}(u(i+1,j,k) - 2u(i,j,k) + u(i-1,j,k)), \tag{15e}$$

$$u_{yy}(i,j,k) = \frac{1}{\Delta y^2}(u(i,j+1,k) - 2u(i,j,k) + u(i,j-1,k)), \tag{15f}$$

$$\begin{aligned} u_{xy}(i,j,k) = \frac{1}{4\Delta x\Delta y}(&u(i+1,j+1,k) - u(i-1,j+1,k) \\ &- u(i+1,j-1,k) + u(i-1,j-1,k)), \end{aligned} \tag{15g}$$

and analogously for v.

We also need the discretisation of u_{tt} (and similarly the discretisation of v_{tt}):

$$u_{tt}(i,j,k) = \frac{1}{(\Delta t)^2}(u(i,j,k+1) - 2u(i,j,k) + u(i,j,k-1)). \tag{16}$$

Finally, we define

$$f_x(i,j,k) = F(t_k), \quad \text{for} \quad i = 2 \text{ (to bypass the pseudo-node } x_1), \tag{17a}$$

$$f_x(i,j,k) = 0 \quad \text{otherwise}, \tag{17b}$$

$$f_y(i,j,k) = 0, \tag{17c}$$

as we would like to simulate the production of waves on one side of the plate. As showed in the Figure 1, $i = 2$ corresponds to the edge of the plate, while $i = 1$ and $i = N_x + 2$ correspond to the pseudo-nodes used to satisfy the Lamb wave boundary conditions (stress-free surface).

The boundary conditions are implemented by the following equations at the edges of I_x (for inner values of y_j):

$$u(1,j,k) = C\frac{\Delta x}{2\Delta y}(v(2,j+1,k) - v(2,j-1,k)) + u(2,j,k), \tag{18a}$$

$$v(1,j,k) = \frac{\Delta x}{2\Delta y}(u(2,j+1,k) - u(2,j-1,k)) + v(2,j,k), \tag{18b}$$

where $C = (c_L(2,j)^2 - 2c_T(2,j)^2)/c_L(2,j)^2$, and

$$\begin{aligned} u(N_x+2,j,k) = &- C\frac{\Delta x}{2\Delta y}(v(N_x+1,j+1,k) - v(N_x+1,j-1,k)) \\ &+ u(N_x+1,j,k); \end{aligned} \tag{19a}$$

$$\begin{aligned} v(N_x+2,j,k) = &- \frac{\Delta x}{2\Delta y}(u(N_x+1,j+1,k) - u(N_x+1,j-1,k)) \\ &+ v(N_x+1,j,k); \end{aligned} \tag{19b}$$

where $C = (c_L(N_x+1,j)^2 - 2c_T(N_x+1,j)^2)/c_L(N_x+1,j)^2$ and the following equations at the edges of I_y (for inner values of x_i):

$$u(i,1,k) = \frac{\Delta y}{2\Delta x}(v(i+1,2,k) - v(i-1,2,k)) + u(i,2,k), \tag{20a}$$

$$v(i,1,k) = C\frac{\Delta y}{2\Delta x}(u(i+1,2,k) - u(i-1,2,k)) + v(i,2,k), \tag{20b}$$

where $C = (c_L(i,2)^2 - 2c_T(i,2)^2)/c_L(i,2)^2$, and

$$\begin{aligned} u(i,N_y+2,k) = &- \frac{\Delta y}{2\Delta x}(v(i+1,N_y+1,k) - v(i-1,N_y+1,k)) \\ &+ u(i,N_y+1,k); \end{aligned} \tag{21a}$$

$$\begin{aligned} v(i,N_y+2,k) = &- C\frac{\Delta y}{2\Delta x}(u(i+1,N_y+1,k) - u(i-1,N_y+1,k)) \\ &+ v(i,N_y+1,k); \end{aligned} \tag{21b}$$

where $C = (c_L(i,N_y+1)^2 - 2c_T(i,N_y+1)^2)/c_L(i,N_y+1)^2$

In the system of equations (7) we can replace derivatives by the above approximations, and get an evolutionary system of two algebraic equations (plus the boundary conditions). The system will be of the form

$$u(i,j,k+1) = F_u(u(*,*,k), v(*,*,k), u(*,*,k-1), v(*,*,k-1)), \quad (22a)$$
$$v(i,j,k+1) = F_v(u(*,*,k), v(*,*,k), u(*,*,k-1), v(*,*,k-1)), \quad (22b)$$

where F_u and F_v are two linear functions of the arguments, and the '*' stand for the suitable space grid points, which allows to find the values of u and v on the space grid points (x_i, y_j) at the time t_{k+1} given all values of u and v on the space grid points (x_i, y_j) at the times t_k, t_{k-1}.

4. Experimental Set-up

The specimen adopted for the experimental campaign is a SLJ made of two aluminium plates (630 mm × 126 mm × 1.2 mm) with an overlap of 30 mm (Figure 2). Here teflon film (length *Deb*) is applied in order to reduce

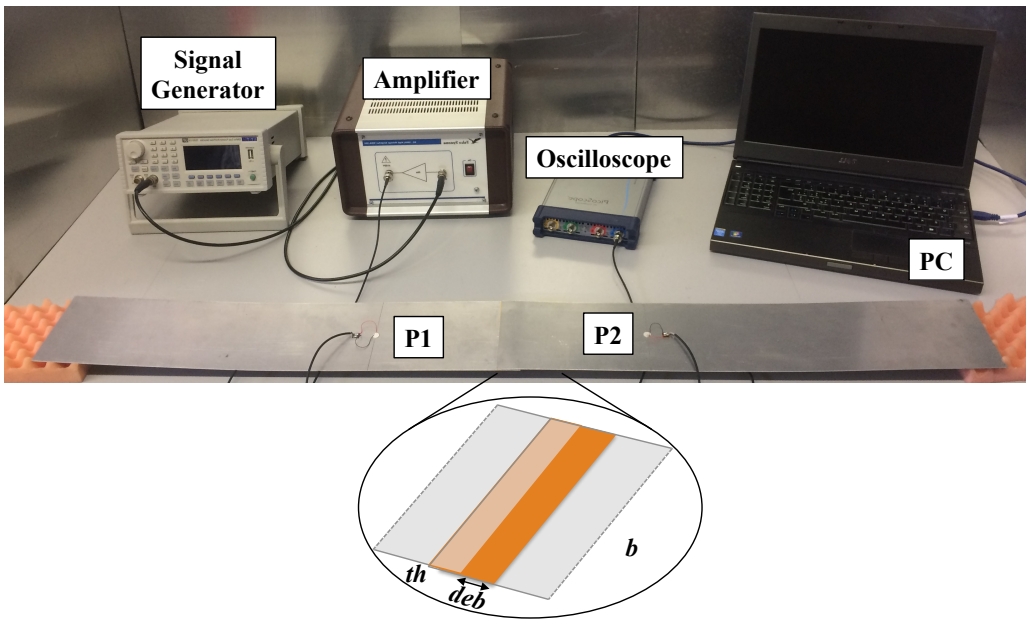

Figure 2: Experimental set-up

the adhesive zone (length l) to simulate a disbond damage: six identical samples are manufactured, using increasing values of debonding (3 – 5 – 7.5 – 10 – 12.5 – 15 mm). The proposed method works only for complete

debonding along the side b, with deb not varying along the b dimension. In other terms, the approach is bidimensional. This limitation, indeed, does not affect the relevance of the approach: this 2D model, on one hand, is of practical interest for all the structural applications involving beamlike structures (for which most of the debondings are expected to be of the kind herein treated); on the other hand, it represents the benchmark for a more complex extension to 3D models, where the geometries and the equations are much more complicated than the ones reported in this paper.

During the experimental tests, stress-free conditions are achieved using vibration-absorbing sponge under the free short edge and overlapped zone of the SLJ. In Figure 3 the overall experimental process is illustrated

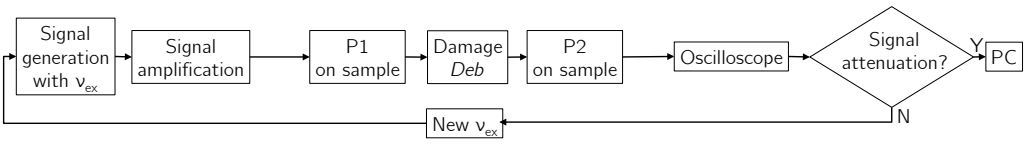

Figure 3: Schematic of the experimental set–up

while in Figure 2 the experimental set–up is presented (see also [4], where other methods different from those presented in this work were discussed). The exciting input to the sample (tone burst with N_i peaks and exciting frequency ν_{ex}) is provided by the signal generator TG5012A of Aim & Thurlby Thandar Instrument and powered (multiplying by 50 the input voltage) by Falco System WMA – 300, feeding the exciting piezo-sensor P1 with low harmonic distortion – low phase noise – high frequency resolution; the signal excites the overlap zone and comes into the receiver sensor P2, that is connected to the oscilloscope Serie 3000 PicoScope. With Single Trigger mode control, the scope monitors the incoming signal and waits for the voltage to rise above a given threshold (variable for each disbond length); then, it causes the scope to capture and display just the first received waveform on P2. All signals are low-pass filtered and processed using software PicoScope 6 and MATLAB codes on PC in order to detect the differences for the various investigated disbond lengths. This real-time acquisition of the propagating waveforms allows to monitor the output signal: ν_{ex} must be changed as long as the P2 signal does not contain changes, suggesting the presence of damage in the overlap zone, in terms of waveform (Figure 4–left graphs) and frequency spectrum (Figure 4–right graphs, obtained by FFT of the transient acquired packets).

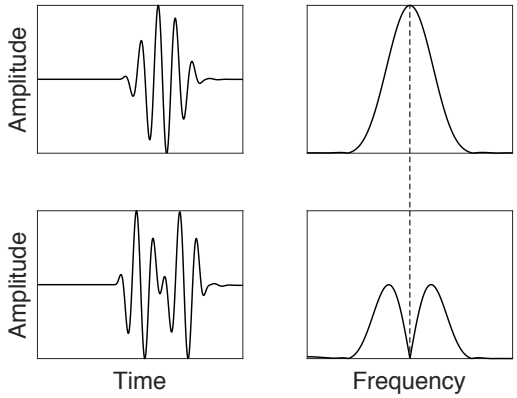

Figure 4: Output signal post-processing (top: signal without amplitude attenuation; bottom: signal with amplitude attenuation)

5. Results

In the Table 1 for each disbond Deb the value of N_i that is required in order to have destructive interference with exciting frequency $\nu^*_{ex} = \nu_{att}$ is reported. λ_{att} is the signal wave length computed using the longitudinal

Table 1: Numerical and experimental results

Deb [mm]	N_i	Num. Results		Exp. Results		Deb_{ev} [mm]	Error [%]
		ν_{att} [kHz]	λ_{att} [mm]	ν_{att} [kHz]	λ_{att} [mm]		
3	8	357	14.1	344	14.6	3.4	13.1
5	5	225	22.4	230	21.9	5.1	1.5
7.5		154	32.7	155	32.5	7.6	0.4
10		118	42.6	116	43.4	10.1	0.6
12.5		92	54.7	95	52.9	12.4	-1.7
15	3	79	63.7	87	57.8	13.5	-10.6

wave velocity in aluminum sample (5030 m/s in Figure 5 and 6). This value was obtained by resolving the Rayleigh-Lamb equation in MATLAB. A very slightly dispersive behaviour can be observed between the used frequency ($\nu th = 0.0948$ MHzmm for ν_{att} equal to 79 kHz and $\nu th = 0.4284$ MHzmm for ν_{att} equal to 357 kHz) in curves of Figure 5 (wave velocity dispersion curves) and Figure 6 (group velocity dispersion curves).

From Table 1 the following conclusions can be formulated: (i) disbond length smaller than 3 mm and bigger than 15 mm were not taken into

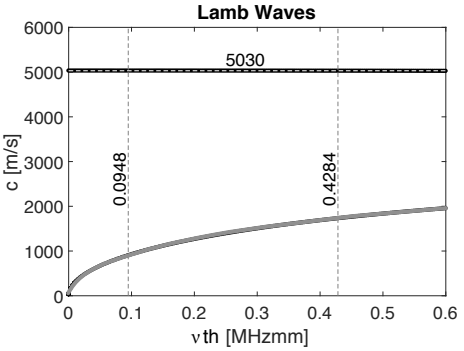

Figure 5: Wave speed dispersion for aluminum plate (S0 in black and A0 in grey)

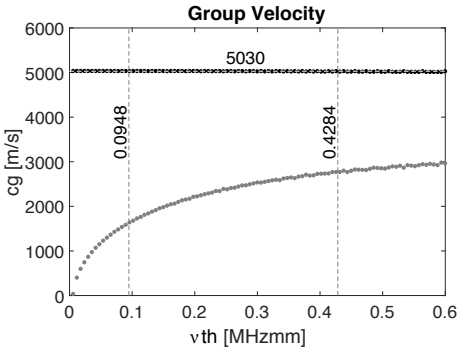

Figure 6: Wave speed group dispersion for aluminum plate (S0 in black and A0 in grey)

account since they look far from practical interest; (ii) for a proper combination of number of peaks and debonding length, there is a specific exciting frequency ν_{att} characterised by attenuated amplitude signal; (iii) increasing the disbond length results in a linear increase of λ_{att} (see Figure 14); (iv) there is a strong correlation between numerical and experimental results, in terms of Deb_{ev} (see 10% error bar in Figure 14). In Figure 7a)

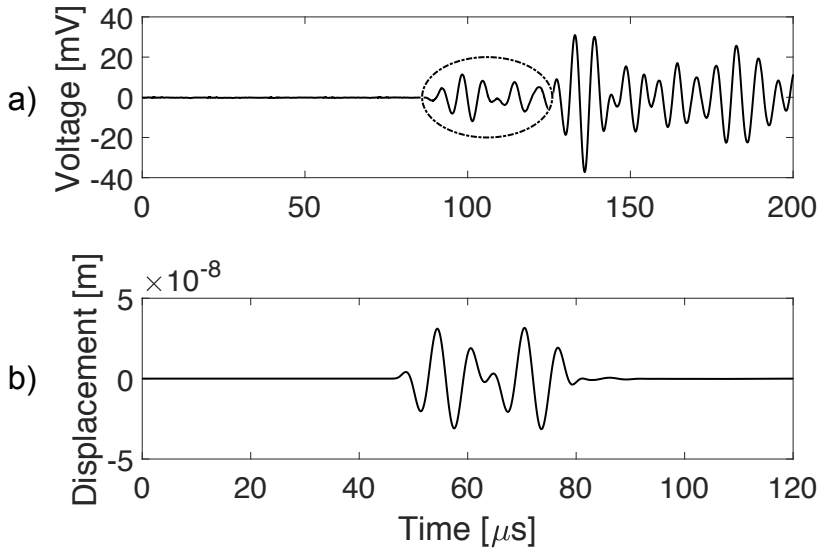

Figure 7: Experimental a) and numerical b) signals obtained by using a 5-peaks toneburst at 155 kHz for a disbond length of 7.5 mm

a typical experimental signal acquired in PZT–2 is reported: the dotted

circle includes the part of the signal showing the attenuation due to the destructive interference. All the remaining part is the result of the reflection on the sample boundaries. The numerical simulations, being the result of a two-dimensional model, provide a signal without reflections like the one presented in Figure 7b).

In the Figures from 8 to 13, FFT of the transient acquired signals (grey scale) and the numerical simulations (black scale), windowed at the packet arrival time, are reported for the different conditions of destructive interference related to the different values of disbond. Whilst the output of

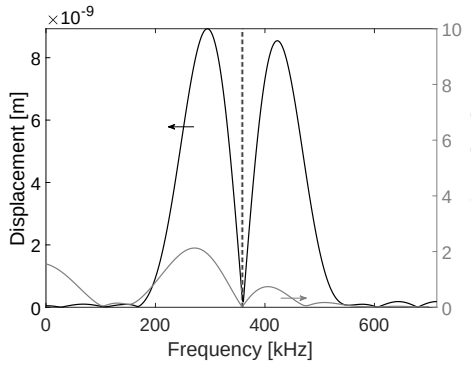

Figure 8: Deb = 3 mm: experiment vs numerical model

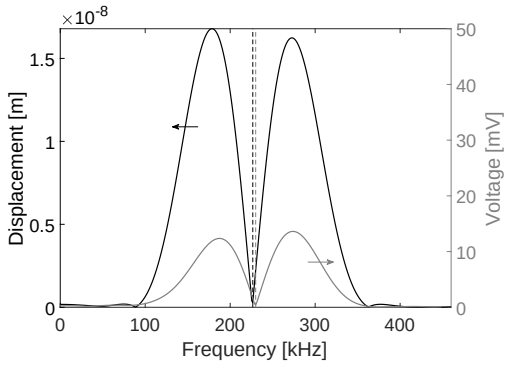

Figure 9: Deb = 5 mm: experiment vs numerical model

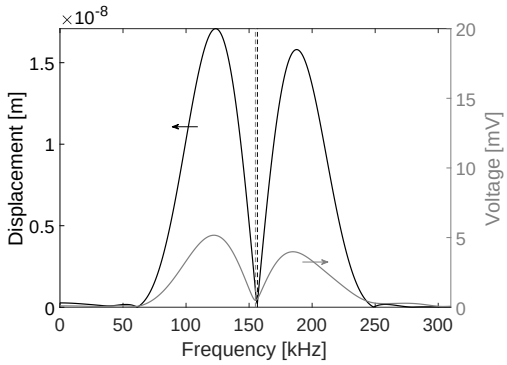

Figure 10: Deb = 7.5 mm: experiment vs numerical model

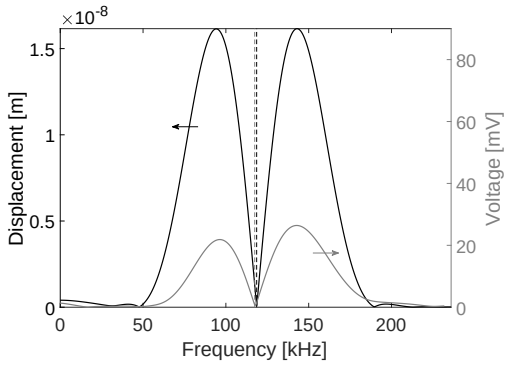

Figure 11: Deb=10 mm: experiment vs numerical model

the numerical model is a displacement vector field ([m]), the experimental post-processing works with P2 signal ([mV]). The destructive interference, clearly represented in the numerical and experimental plots, is characterised

by a strong amplitude attenuation at the exciting frequency ν_{att} (vertical dotted line in Figures) related to the specific value of disbond. The shape of the attenuated signals deviate from the bell-shape (Figure 4) of the original excitation.

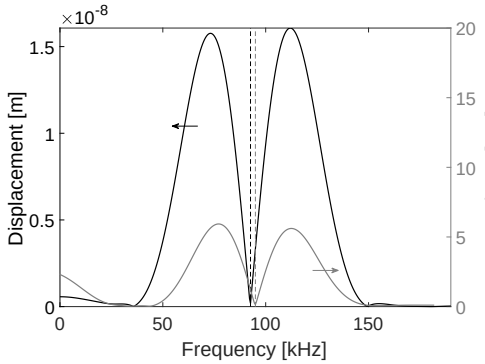

Figure 12: Deb=12.5 mm: experiment vs numerical model

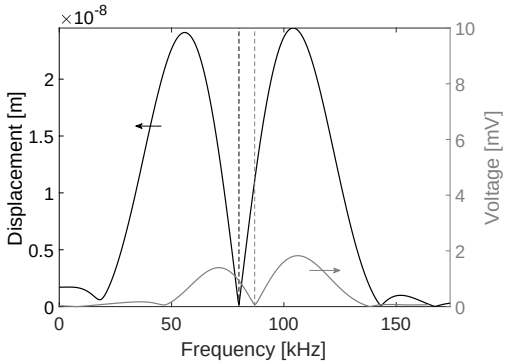

Figure 13: Deb=15 mm: experiment vs numerical model

These plots are characterised by cusps that mean frequency values with very low amplitude and assume a two bell-shape frequency spectrum. From these Figures it is possible to highlight a high correlation between numerical and experimental results confirming what provided by Table 1. The error is below 10% except for the case with 15 mm (which represents the 50% of the total bond length) and 3 mm of debonding.

In Figure 14 the numerical wave lengths, in circle markers, are reported with a linear interpolation formula (intercept equal to zero and dotted line in Figure); experimental results are reported in diamond markers. The slope value, SLJ specific feature, is used to evaluate the debonding length Deb_{ev} (coming from experimental wave lengths λ_{att}).

Experiments and numerical simulations were performed using toneburst with central frequency other than ν_{att}. For these situations the wave packet preserved the original profile (and thus the frequency spectrum). These results were not reported in the paper for the sake of conciseness.

6. Conclusions

This article presents a novel numerical model for wave motion in media with space dependent properties. Cauchy–Navier's equations for elastodynamics were solved, in terms of finite differences, for a thin plate (SLJ)

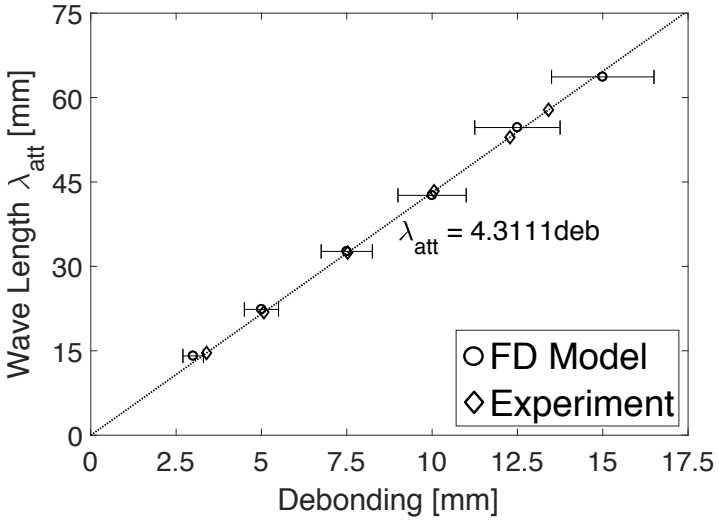

Figure 14: Debonding, attenuation wave length chart

excited by Lamb waves. The presence of an overlap zone with damage (debonding) was simulated with a piecewise-constant function describing the wave propagation velocity (dependent on the density). Modulated tone bursts were used to excite the joint and this excitation was modelled by a source point in the finite differences model. The joint spectral response was carefully investigated to relate the damage, artificially realised, with the signal content. Numerical simulations and experimental campaigns were conducted to validate the developed model and signal attenuation at specific frequencies for each value of disbond was found representative of the damage. Every frequency ν_{att} was associated with a wave length in the attenuated signal: a linear relationship between λ_{att} and Deb was found.

It is worth to remark that the observed coincidence of numerical simulations and experimental results occurs in spite of the more simple geometry of the numerical model. This is probably due to the presence of a discrete symmetry property of the solution across the bonded region. However, at the moment this statement shall be regarded as a conjecture as a mathematical proof o it is yet to be found.

There are several reasons that make the method interesting. First of all, the method based on a Finite Difference modelling is relatively simple. Numerical simulations like the ones presented in this manuscript can be implemented in any programming language (Matlab was used, but Octave would do the same job and is free) and run on any computer, as they are

not resource-consuming. Then, the proposed approach reveals the damage length by using particular exciting frequencies. In the authors' opinion, the elegance, simplicity and low cost of the method make it particularly interesting for industrial applications.

Acknowledgements

The ahthors are grateful to G. Saccomandi and K. Khusnutdinova for useful suggestions. This research has been supported by the Department of Innovation Engineering and Department of Mathematics and Physics of the Università del Salento. RV also acknowledges the support of GNFM of the Istituto Nazionale di Alta Matematica (Italy) and of the Italian National Institute for Nuclear Physics INFN, IS-CSN4 *Mathematical Methods of Nonlinear Physics*.

References

[1] Alterman, Z., Loewenthal, D., 1970. Seismic waves in a quarter and three-quarter plane. Geophysical Journal of the Royal Astronomical Society 20 (2), 101–126, http://dx.doi.org/10.1111/j.1365-246X.1970.tb06058.x.

[2] Balasubramanyam, R., Quinney, D., Challis, R., Todd, C., 1996. A finite-difference simulation of ultrasonic Lamb waves in metal sheets with experimental verification. Journal of Physics D: Applied Physics 29 (1), 147, https://doi.org/10.1088/0022-3727/29/1/024.

[3] Balvantín, A. J., Diosdado-De-la-Peña, J. A., Limon-Leyva, P. A. and Hernández-Rodríguez, E., 2018. Study of guided wave propagation on a plate between two solid bodies with imperfect contact conditions. Ultrasonics, 83, 137–145, https://doi.org/10.1016/j.ultras.2017.06.003

[4] Carrino, S., Nicassio, F., Scarselli, G., 2018. SHM of aerospace bonded structures with improved techniques based on NEWS. In: Health Monitoring of Structural and Biological Systems XII. Vol. 10600. International Society for Optics and Photonics, p. 106002B, https://doi.org/10.1117/12.2300350.

[5] Dreiden, G V and Khusnutdinova, K R and Samsonov, A V and Semenova, I V (2012). Bulk strain solitary waves in bonded layered polymeric bars with delamination. J. Appl. Phys. 112, 063516, http://dx.doi.org/10.1063/1.4752713.

[6] Donskoy, D., Sutin, A., Ekimov, A., 2001. Nonlinear acoustic interaction on contact interfaces and its use for nondestructive testing. Ndt & E International 34 (4), 231–238, https://doi.org/10.1016/S0963-8695(00)00063-3.

[7] Fan, Z., Lowe, M. J., 2009. Elastic waves guided by a welded joint in a plate. In: Proceedings of the Royal Society of London A: Mathematical, Physical and Engineering Sciences. The Royal Society, pp. rspa–2009, https://doi.org/10.1098/rspa.2009.0010.

[8] Ginzburg, D., Ciampa, F., Scarselli, G., Meo, M., 2017. SHM of single lap adhesive joints using subharmonic frequencies. Smart Materials and Structures 26 (10), 105018, https://doi.org/10.1088/1361-665X/aa815c.

[9] Giurgiutiu, V., 2014. Wave Propagation SHM with PWAS Transducers. In: Structural Health Monitoring with Piezoelectric Wafer Active Sensors: with Piezoelectric Wafer Active Sensors. Elsevier, pp. 639–706, https://doi.org/10.1016/C2013-0-00155-7.

[10] Gurtin, M. E., 1973. The linear theory of elasticity. In: Linear theories of elasticity and thermoelasticity. Springer, pp. 1–295, http://dx.doi.org/10.1007/978-3-662-39776-3_1.

[11] Heidarpour, F., Farahani, M., Ghabezi, P., 2018. Experimental investigation of the effects of adhesive defects on the single lap joint strength. International journal of adhesion and adhesives 80, 128–132, https://doi.org/10.1016/j.ijadhadh.2017.08.005.

[12] Huthwaite, P., 2016. Guided wave tomography with an improved scattering model. Proc. R. Soc. A 472 (2195), 20160643, https://doi.org/10.1098/rspa.2016.0643.

[13] Jankauskas, A., Mazeika, L., 2016. Ultrasonic guided wave propagation through welded lap joints. Metals 6 (12), 315, https://doi.org/10.3390/met6120315.

[14] Jin, J., Quek, S., Wang, Q., 2003. Analytical solution of excitation of Lamb waves in plates by inter-digital transducers. In: Proceedings of the Royal Society of London A: Mathematical, Physical and Engineering Sciences. Vol. 459. The Royal Society, pp. 1117–1134, https://doi.org/10.1098/rspa.2002.1071.

[15] Kalkowski, M. K., Rustighi, E., Waters, T. P., 2016. Modelling piezoelectric excitation in waveguides using the semi-analytical finite element method. Computers & Structures 1, 173–186. https://doi.org/10.1016/j.compstruc.2016.05.022.

[16] Khusnutdinova, K. R., Samsonov, A. M., 2008. Fission of a longitudinal strain solitary wave in a delaminated bar. Phys. Rev. E 77, 066603, https://doi.org/10.1103/PhysRevE.77.066603.

[17] Khusnutdinova, K. R, Tranter, M. R., 2018. On radiating solitary waves in bi-layers with delamination and coupled Ostrovsky equations. Chaos, 27, 013112, http://dx.doi.org/10.1063/1.4973854.

[18] Khusnutdinova, K. R, Tranter, M. R., 2015. Modelling of nonlinear wave scattering in a delaminated elastic bar. Proc. R. Soc. A, 471, 20150584, http://dx.doi.org/10.1098/rspa.2015.0584.

[19] Kijanka, P., Manohar, A., Lanza di Scalea, F., 2015. Damage location by ultrasonic Lamb waves and piezoelectric rosettes. Journal of Intelligent Material Systems and Structures, 26, 12, https://doi.org/10.1177/1045389X14544140

[20] Kim, Y., Ha, S. and Chang, F. K., 2008. Time-domain spectral element method for built-in piezoelectric-actuator-induced lamb wave propagation analysis. AIAA journal, 46 (3), 591–600, https://doi.org/10.2514/1.27046.

[21] Léonard, F., Stein, J., Soutis, C., Withers, P., 2017. The quantification of impact damage distribution in composite laminates by analysis of X-ray computed tomograms. Composites Science and Technology 152, 139–148, https://doi.org/10.1016/j.compscitech.2017.08.034.

[22] Liu, X., Zhou, L., Ouyang, Q., 2016. Modeling of PZT-induced Lamb wave propagation in structures by using a novel two-layer spectral finite element. In: Sensors and Smart Structures Technologies for Civil, Mechanical, and Aerospace Systems. Vol. 9803. International Society for Optics and Photonics, p. 98034D,

https://doi.org/10.1117/12.2218960.
[23] Mahapatra, D. R. and Gopalakrishnan, S., 2004. Spectral finite element analysis of coupled wave propagation in composite beams with multiple delaminations and strip inclusions. International journal of solids and structures, 41(5–6), 1173–1208, https://doi.org/10.1016/j.ijsolstr.2003.10.018.
[24] Malinowski, P. H., Ostachowicz, W. M., Brune, K., Schlag, M., 2017. Study of electromechanical impedance changes caused by modifications of CFRP adhesive bonds. Fatigue & Fracture of Engineering Materials & Structures 40 (10), 1592–1600, https://doi.org/10.1111/ffe.12661.
[25] Marks, R., Clarke, A., Featherston, C., Paget, C., Pullin, R., 2016. Lamb wave interaction with adhesively bonded stiffeners and disbonds using 3D vibrometry. Applied Sciences 6 (1), 12, https://doi.org/10.3390/app6010012.
[26] Montinaro, N., Cerniglia, D., Pitarresi, G., 2017. Detection and characterisation of disbonds on fibre metal laminate hybrid composites by flying laser spot thermography. Composites Part B: Engineering 108, 164–173, https://doi.org/10.1016/j.compositesb.2016.09.084.
[27] Mueller, E. M., Starnes, S., Strickland, N., Kenny, P., Williams, C., 2016. The detection, inspection, and failure analysis of a composite wing skin defect on a tactical aircraft. Composite Structures 145, 186–193, https://doi.org/10.1016/j.compstruct.2016.02.046.
[28] Ong, W. H., Rajic, N., Chiu, W. K., Rosalie, C., 2018. Lamb wave–based detection of a controlled disbond in a lap joint. Structural Health Monitoring 17 (3), 668–683, https://doi.org/10.1177/1475921717715302.
[29] Ren, B., Lissenden, C. J., 2018. Modeling guided wave excitation in plates with surface mounted piezoelectric elements: coupled physics and normal mode expansion. Smart Materials and Structures 27 (4), 045014, https://doi.org/10.1088/1361-665X/aab162.
[30] Scarselli, G., Ciampa, F., Nicassio, F., Meo, M., 2017. Non-linear methods based on ultrasonic waves to analyse disbonds in single lap joints. Proceedings of the Institution of Mechanical Engineers, Part C: Journal of Mechanical Engineering Science 231 (16), 3066–3076, https://doi.org/10.1177/0954406217704222.
[31] Scarselli, G., Corcione, C., Nicassio, F., Maffezzoli, A., 2017. Adhesive joints with improved mechanical properties for aerospace applications. International Journal of Adhesion and Adhesives 75, 174–180, https://doi.org/10.1016/j.ijadhadh.2017.03.012.
[32] Scarselli, G., Nicassio, F., 2017. Analysis of debonding in single lap joints based on employment of ultrasounds. In: Health Monitoring of Structural and Biological Systems 2017. Vol. 10170. International Society for Optics and Photonics, p. 1017020, https://doi.org/10.1117/12.2260041.
[33] Solodov, I., Bai, J., Bekgulyan, S., Busse, G., 2011. A local defect resonance to enhance acoustic wave-defect interaction in ultrasonic nondestructive evaluation. Applied Physics Letters 99 (21), 211911, https://doi.org/10.1063/1.3663872.
[34] Solodov, I. Y., Krohn, N., Busse, G., 2002. CAN: an example of nonclassical acoustic nonlinearity in solids. Ultrasonics 40 (1-8), 621–625, https://doi.org/10.1016/S0041-624X(02)00186-5.
[35] Yadav, V. B., Pramila, T., Raghuram, V., Kishore, N., 2006. A finite difference simu-

lation of multi-mode Lamb waves in aluminium sheet with experimental verification using laser based ultrasonic generation. In: Proceedings of the 12th Asia-Pacific conference on NDT. Citeseer, pp. 1–7.

[36] Yashiro, S., Wada, J., Sakaida, Y., 2017. A monitoring technique for disbond area in carbon fiber–reinforced polymer bonded joints using embedded fiber Bragg grating sensors: Development and experimental validation. Structural Health Monitoring 16 (2), 185–201, https://doi.org/10.1177/1475921716669979.